Hydrogen storage in Mg–LiBH$_4$ composites catalyzed by FeF$_3$

CrossMark

Julián Puszkiel [a, b, *], Fabiana C. Gennari [a], Pierre Arneodo Larochette [a], Horacio E. Troiani [a],
Fahim Karimi [b], Claudio Pistidda [b], Rapee Gosalawit–Utke [b, c], Julian Jepsen [b],
Torben R. Jensen [d], Carsten Gundlach [e], Martin Tolkiehn [f], José Bellosta von Colbe [b],
Thomas Klassen [b], Martin Dornheim [b]

[a] Instituto Balseiro (UNCuyo and CNEA), Consejo Nacional de Investigaciones Científicas y Técnicas, (CONICET) and Centro Atómico Bariloche,
Av. Bustillo km 9.5, R8402AGP S. C. de Bariloche, Argentina
[b] Institute of Materials Research, Helmholtz–Zentrum Geesthacht, Centre for Materials and Coastal Research GmbH, D-21502 Geesthacht, Germany
[c] School of Chemistry, Institute of Science, Suranaree University of Technology, Nakhon Ratchasima 30000, Thailand
[d] Center for Energy Materials, iNANO and Department of Chemistry, University of Aarhus, Aarhus C8000, Denmark
[e] MAX-lab, Lund University, S-22100 Lund, Sweden
[f] HASYLAB at DESY, Notkestraße 85, D-22603 Hamburg, Germany

HIGHLIGHTS

- The effect of FeF$_3$ on the Mg–10 mol%LiBH$_4$ is investigated.
- Mg–10 mol%LiBH$_4$ + 5 mol% FeF$_3$ shows improved dehydrogenation kinetic properties.
- In-situ formation of the FeB species is detected.

ABSTRACT

Mg–10 mol% LiBH$_4$ composite plus small amounts of FeF$_3$ is investigated in the present work. The presence of LiBH$_4$ during the milling process noticeably modifies the size and morphology of the Mg agglomerates, leading to faster hydrogenation and reaching almost the theoretical hydrogen capacity owing to enhanced hydrogen diffusion mechanism. However, the dehydrogenation of the system at low temperatures ($\leq$300 °C) is still slow. Thus, FeF$_3$ addition is proposed to improve the dehydrogenation kinetic behavior. From experimental results, it is found that the presence of FeF$_3$ results in an additional size reduction of the Mg agglomerates between ~10 and ~100 μm and the formation of stable phases such as MgF$_2$, LiF and FeB. The FeB species might have a catalytic effect upon the MgH$_2$ decomposition. As a further result of the FeF$_3$ addition, the Mg–10 mol%LiBH$_4$–5 mol% FeF$_3$ material shows improved dehydrogenation properties: reduced dehydrogenation activation energy, faster hydrogen desorption rate and reversible hydrogen capacities of about 5 wt% at 275 °C.

© 2014 Elsevier B.V. All rights reserved.

1. Introduction

The design of adequate materials for hydrogen storage is the main challenge for application of the "hydrogen economy" to the transport sector. Metal hydrides, complex hydrides and nanotubes, among others, have been investigated as hydrogen carriers [1–6].

Despite all the effort put in improving such solid materials, unfortunately none of the available candidate storage materials meet the DOE technical targets, which involve reversible hydrogen capacity of 1.8 kWh kg (>6 wt% H; year 2017) at moderates pressures and temperatures with fast de/hydrogenation kinetics, high cycle stability, low enthalpy effects and low cost [7].

In particular, MgH$_2$ has high reversible storage capacity (7.6 wt% H) and low cost; but the main drawback is that its high enthalpy does not allow low desorption temperatures (<300 °C). Several investigations showed that the hydrogen storage capacity and kinetic behavior of MgH$_2$ can be improved by applying different strategies such as the synthesis of nanocrystalline hydrides through

high energy mechanical milling, the addition of catalysts such as transition metal oxides and halides and the combination of MgH_2 plus complex hydrides with light weight elements, mainly with $LiBH_4$ due to its high hydrogen content of 18.3 wt% H [8–30].

Johnson et al. [13] and Mao et al. [14] obtained enhanced hydrogen absorption kinetic properties at low temperatures for Mg via the addition of small amounts of $LiBH_4$. Microstructural, morphological and thermal analyses showed that the MM of Mg + 10 mol% $LiBH_4$ material in argon atmosphere results in a physical mixture of Mg and $LiBH_4$ with small agglomerate size distributions from 10 μm to 170 μm and grain sizes of roughly 20 nm for Mg [16,17]. Investigations on the kinetic and thermodynamic properties of the Mg + 10 mol% $LiBH_4$ material led to the conclusion that the addition of $LiBH_4$ to Mg has neither catalytic effect on the hydrogen sorption properties of MgH_2, nor influence on thermodynamic behavior of the Mg–MgH_2 hydride system, respectively. However, improved hydrogen absorption kinetic properties mainly at low temperatures (300 °C) were noticed. This behavior was attributed to the high degree of microstructural refinement and Mg agglomerates with irregular surfaces which provide shorter diffusion paths for hydrogen and more specific surface for the Mg and H interaction [16,17]. Despite the fact that the Mg + 10 mol% $LiBH_4$ material presented improved hydrogen absorption kinetic properties at 300 °C, its hydrogen desorption rate was still slow.

It was observed that transition metal oxides and halides reduce the temperature and speed up the rate of MgH_2 decomposition [18–30]. Oelerich et al. and Barkhordarian et al. [19–21] showed that transition metal oxides have a beneficial effect on the MgH_2 sorption kinetic behavior. It was reported that Nb_2O_5 is the most effective oxide to speed up the hydrogen sorption of MgH_2 at a low temperature of 250 °C [20,21]. Deledda et al. [23] found that the addition of 5 mol% FeF_3 reduces the desorption temperature of MgH_2 up to 230 °C and shortens the hydrogen release times to 500 s at 300 °C. Moreover, Yavari et al. [24] also reached lower desorption temperature of 250 °C and faster decomposition rates for MgH_2 by the addition of 3 mol% of FeF_3. This enhanced desorption behavior of MgH_2 was attributed to the catalytic effect of a highly reactive surface composed of MgF_2 and Fe nanoparticles formed from the MgH_2 and FeF_3 interactions [24,25]. In other works [26–30], the catalytic effect of several transition metal halides such as FeF_2, NiF_2, TiF_3, NbF_5, VF_4, ZrF_4 and CrF_2 upon the kinetic properties of MgH_2 was studied. It was found that Ti, V and Nb halides are more effective than Fe, Zr and Cr halides. Additionally, Ma et al. [30] investigated the differences between the catalytic effects of TiF_3 and $TiCl_3$ upon MgH_2. Based on the experimental results they concluded that fluorine anion has a more effective catalytic effect

than chlorine one. Furthermore, they inferred that fluorine and chlorine interact with Mg in different ways. Transition metal halides also cause destabilizing effects on $LiBH_4$ [31–34]. Adding transition metal halides such as $TiCl_3$, TiF_3 and $MnCl_2$ to $LiBH_4$, it is possible to noticeably reduce the decomposition temperature up to 150 °C [32–35].

The transition metal halides addition can lower the decomposition temperature of both MgH_2 and $LiBH_4$ [22–35] and shorten the hydrogen release times from MgH_2 [23,24]. Therefore, in this work FeF_3 was added to Mg + 10 mol%$LiBH_4$ composite material in order to improve its decomposition kinetic behavior. Applying several experimental techniques and calculations in equilibrium conditions, we investigated the influence of FeF_3 upon the hydrogen sorption kinetic behavior of MgH_2. Furthermore, the interactions between the iron halide and $LiBH_4$ were also analyzed.

2. Experimental

2.1. Material preparation

Mg composite materials were prepared by ball milling in argon atmosphere by using a Fritsch–P6 planetary mill device, an 80 ml milling chamber and ball to powder ratio of 40:1. Moreover, some compounds were also mixed in mortar in order to study their interactions upon heating. As starting materials Mg (Riedel–de Haën, purity > 99.9%), $LiBH_4$ (Sigma–Aldrich, purity ≥ 90%), Fe (Sigma–Aldrich, purity > 99.99%) and FeF_3 (Sigma–Aldrich, purity > 99.99%) were used. In order to work with fresh material and to minimize the formation of species such as oxides, hydroxides, etc., all materials were prepared and stored no more than two weeks in glove boxes with oxygen and moisture controlled atmosphere before performing the measurements and characterizations. In Table 1, the composition expressed in mol%, the preparation procedure and their parameters as well as the used characterization techniques are shown. All the Mg composite materials are designated throughout the paper as shown in Table 1.

2.2. Material characterization

The investigated Mg composite materials during and after the mechanical milling (MM), after hydrogenation and dehydrogenation were characterized using the following techniques: laboratory X–ray diffraction (Lab–PXD), ex-situ and in-situ synchrotron radiation X-ray diffraction (SR–PXD), scanning electron microscopy (SEM) with dispersive X-ray spectroscopy (EDS), high resolution transmission electron microscopy (HR-TEM) with electron diffraction and EDS, differential scanning calorimetry (DSC), Fourier

Table 1
Composition in mol%, designation, preparation procedures and their parameters as well as the used characterization techniques for the investigated materials.

Material (composition in mol%)	Designation	Preparation procedure and parameters	Characterization techniques
90 Mg + 10$LiBH_4$	M10L	Milled for 10 h at 400 rpm	Lab. PXD, DSC, PSD, titration measurements
60 Mg + 40$LiBH_4$	M40L	Milled for 10 h at 400 rpm	Lab. PXD, FT-IR of the solid phase
85 Mg + 10$LiBH_4$ + 5Fe	M10L5Fe	Milled for 10 h at 400 rpm	Lab. PXD, DSC, SEM, PSD, HR-TEM, titration measurements, equilibrium calculations
50 Mg + 40$LiBH_4$ + 10Fe	M40L10Fe	Milled for 10 h at 400 rpm 50 Mg + 40$LiBH_4$ and then 10Fe mixed in mortar	Lab. PXD, FT-IR of the solid phase
85 Mg + 10$LiBH_4$ + 5FeF_3	M10L5FF	Milled for 10 h at 400 rpm	Lab. and SR − PXD, DSC, SEM, HR-TEM, FT-IR of the gas phase, titration measurements, equilibrium calculations
50 Mg + 40$LiBH_4$ + 10FeF_3	M40L10FF	Milled for 10 h at 400 rpm 50 Mg + 40$LiBH_4$ and then 10FeF_3 mixed in mortar	Lab. PXD, in-situ SR − PXD, FT-IR of the solid phase, equilibrium calculations

transform infrared spectroscopy (FT–IR) of the solid and gas phases, particle/agglomerate size distribution analysis (PSD) and the volumetric technique.

2.2.1. Powder X-ray diffraction

Lab PXD (Device: Philips PW 1710/01 Instruments, CuK$_a$ radiation, $\lambda = 1.5405$ Å, graphite monochromator, 30 mA and 40 kV) and ex-situ SR–PXD (Beamline D3 at HASYLAB–DESY, Hamburg, Germany, $\lambda = 0.5$ Å) measurements were carried out for phase identification and grain size calculation by the Scherrer equation for the Mg composite materials after MM, hydrogenation and dehydrogenation [36]. The interactions among Mg, LiBH$_4$ and FeF$_3$ halide upon heating and subsequent hydrogenation under dynamic conditions were studied via in-situ SR–PXD. The in-situ SR–PXD measurements were carried out in the MAX II Synchrotron in Lund, Sweden, at Beamline I711 in the research laboratory MAXlab using an X-ray wavelength of $\lambda = 0.99917$ Å and a Mar 165 CCD detector for data collection [37]. All samples (0.5–2 mg) were airtight encapsulated in a sapphire capillary and then mounted in a specially developed sample holder [38]. The sample holder was connected to the gas system, which was filled with argon and evacuated till vacuum three times before opening the valve to the sample and starting the experiment. All SR–PXD data are reported referring to the scattering vector $q = 4\pi \sin\theta/\lambda$ (Å^{-1}).

2.2.2. Scanning electron microscopy with EDS and particle size distribution

Analyses of the materials' morphology, microstructure and agglomerate size distribution were performed by SEM and PSD. Powder samples dispersed on a stick were characterized by using secondary electrons (SEM–Zeiss DSM 962). All samples were sputtered and then introduced to the microscope by minimizing all room O$_2$ and H$_2$O contact throughout a specially designed procedure [10]. Additionally, compacted powder samples were observed with back scattered electrons (SEM–Nova Nano SEM 230) and EDS analyses were performed. PSD measurements (Mastersizer Micro MAF 5000; range: 0.3–300 μm) were carried out with samples diluted in n-butane and stirred at 2100 rpm.

2.2.3. High resolution transmission electron microscopy with electron diffraction and EDS analyses

HR-TEM and dark field images were taken and combined with the EDS and electron diffraction patterns analyses with a Philips CM200 UT microscope operating at 200 kV. The samples for TEM were prepared by dispersing a small amount of powder in ethanol and then ultrasonicated before depositing a drop of the resulting suspension on a commercial carbon coated copper grid. The samples were exposed a short time to the air before introducing them to the TEM device. In order to identify the Fe species rich zones, point elemental analyses via EDS coupled to the TEM were performed. Moreover, dark field images and electron diffraction patterns were also carried out for phase's identification in the Fe species rich zones.

2.2.4. Differential scanning calorimetry

The thermal behavior of the materials was studied by DSC (TA Instruments 2910 calorimeter) using an argon flow rate of 122 cm^3 min^{-1} and different heating rates of 1, 2, 5, 7, 10, 15 and 25 °C min^{-1}. From the DSC curves, the activation energy (E_a) of the desorption process was calculated by the Kissinger method [39]. Each point in the Kissinger plot was determined as an average of three measurements and the error band calculated.

2.2.5. Fourier transform infrared spectroscopy

FT–IR measurements were done with samples in solid and gas phases. For FT–IR analyses of the solid phase, the sample was mixed with dry KBr in a mortar and then pressed into pellets. Solid-state FT–IR spectra were obtained from 800 to 2700 cm^{-1} (Device: Bruker – Equinox 55). The gas phase obtained during the MM procedures was subtracted and measured by FT–IR in a specially designed cell. Gas-state FT–IR spectra were obtained from 600 to 4000 cm^{-1} (Device: Perkin Elmer – Spectrum 400). Moreover, H$_2$ gas detection analysis (Bacharach combustible gas leak detector) for the milling chamber atmosphere after MM was also performed.

2.2.6. Titration measurements

The hydrogen kinetic behavior of the Mg composite materials was assessed in a Sieverts kind device with mass flow controllers [40]. All the samples were first heated till 350 °C and then stabilized throughout successive hydrogen absorption–desorption cycles at 350 °C under 2.5 and 0.02 MPa of hydrogen, respectively, so that reproducible kinetic behavior was obtained. Finally, the hydrogen absorption and desorption rates were measured at 325, 300, 275 and 250 °C under 2.5 and 0.02 MPa of hydrogen, respectively. For the sake of clarity, just the hydrogenation–dehydrogenation cycle at 275 °C for the M10L, M10L5Fe and M10L5FF was shown because it is the minimum temperature at which all the samples release hydrogen. To carry out each measurement roughly 100 mg of material was used in order to minimize the heat and mass transfer problems through the powder bed [10,41].

2.3. Material handling

All material handling was carried out in MBraun Unilab golve boxes with oxygen and moisture controlled atmosphere (<10 ppm of O$_2$ and H$_2$O), so as to prevent the oxidation of the samples.

2.4. Thermodynamic calculations

The HSC Chemistry software [42] was used to evaluate the reactivity of the Mg composite materials under different conditions. The most favorable reactions were identified through a combination of Gibbs minimization equilibrium with selected solid and gas species. The obtained results represent ideal phase equilibrium compositions used to predict possible solid products, particularly those which are amorphous, and gaseous species.

3. Results and discussion

3.1. Investigations on the interactions during milling, non-isothermal process and hydrogen cycling

In this section the interactions among Mg–LiBH$_4$ composite material and FeF$_3$ during milling, heating and hydrogen cycling are studied. These interactions are investigated via Lab–PXD, ex- and in-situ SR–PXD, DSC, FT–IR of the gas formed phases and equilibrium composition calculations.

In Fig. 1, the PXD (Fig 1(A and C)) and DSC (Fig. 1(B)) of as-milled M10L, M10L5Fe and M10L5FF are shown. The PXD patterns of M10L (Fig. 1A (a)) and M10L5Fe (Fig. 1A (b)) exhibit reflections coming from the starting materials, i.e. Mg, LiBH$_4$ and Fe. Moreover, in the DSC curves of LiBH$_4$, M10L and M10L5Fe (Fig. 1B (a) and (b)) endothermic events corresponding to the structural transition (105–120 °C) and melting (270–280 °C) of LiBH$_4$ are just observed [43,44]. Thus, after milling, M10L and M10L5Fe materials result in a physical mixture of the starting materials [9,10]. The PXD pattern of M10L5FF after milling (Fig. 1A (c)) shows a small reflection (~28°)
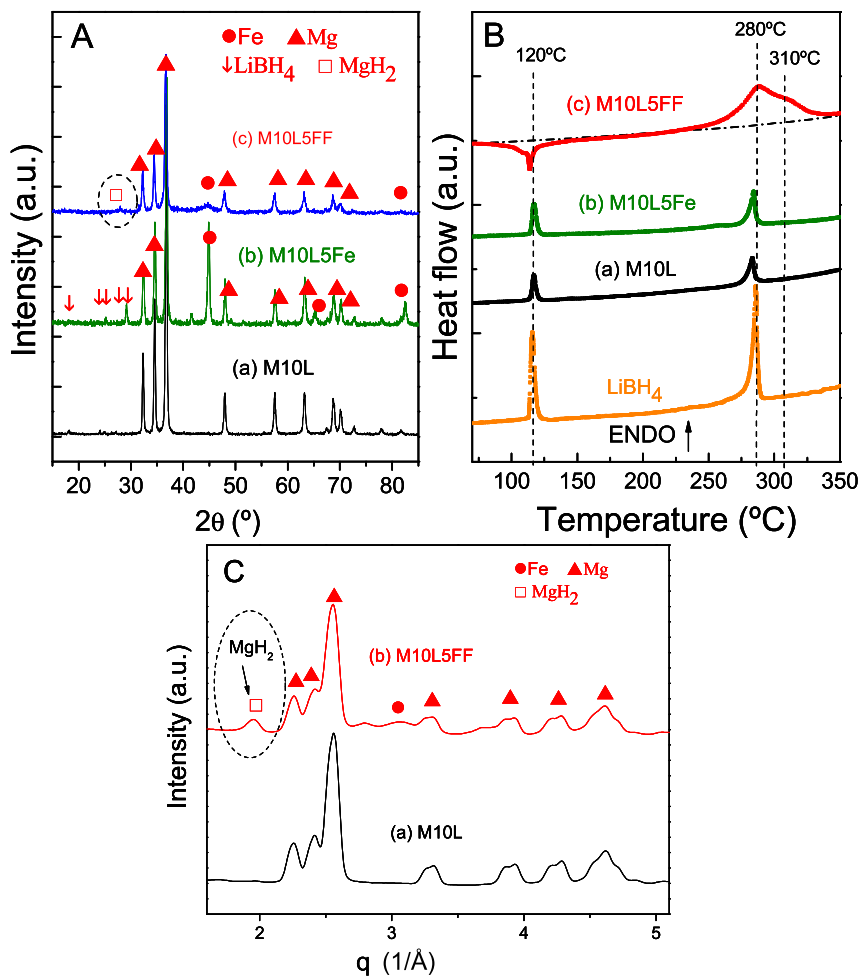
Fig. 1. PXD and DSC analyses of the materials after milling. A − Lab-PXD and B − DSC of (a) M10L, (b) M10L5Fe and (c) M10L5FF (5 °C min^{-1} and 122 cm^3 min^{-1} of Ar). C − Ex−situ SR−PXD for (a) M10L and (b) M10L5FF (HASYLAB − DESY, Hamburg, Germany, $\lambda = 0.5$ Å).

attributed to the presence of MgH$_2$. Additionally, in the ex-situ SR-PXD measurements of the as-milled M10L5FF (Fig. 1C(b)) the presence of MgH$_2$ can be also observed.

FT−IR and H$_2$ detection analyses of the gas phase in the milling chamber for the M10L5FF material after milling have been performed. The FT−IR spectra (not shown) do not exhibit the presence of any volatile molecule (mainly B$_2$H$_6$ and other boron hydrides have been checked). The H$_2$ detection analysis clearly evidences the presence of H$_2$ inside the milling chamber after MM. Zhang et al. [45] studied the gas phase composition via mass spectroscopy (MS) during the non-isothermal decomposition of a LiBH$_4$−SiO$_2$−TiF$_3$ composite from 50 to 550 °C. They found that B$_2$H$_6$ was not present and the gas phase was only composed of H$_{2(g)}$. Taking into account that the MM processes have been performed in argon atmosphere, these results hint that the energy imparted during milling (by the grinding medium) to the M10L5FF is enough to make possible some interactions.

In the DSC curve of the as-milled M10L5FF (Fig. 1B(c)) differences regarding the M10L and M10L5Fe materials (Fig. 1B (a) and (b)) are also noticed. For M10L5FF (Fig. 1B (c)), an exothermic event between 90 and 150 °C and an endothermic event between 250 and 340 °C are seen. This endothermic event presents a peak maximum at 280 °C and then a bump at 310 °C (Fig. 1B (c)). This behavior suggests that two thermal processes are overlapping between 250 and 340 °C.

After hydrogenation-dehydrogenation cycling, PXD and DSC analyses of hydrided and dehydrided samples in different conditions (Fig. 2(A and B)) have been carried out. In Fig. 2A (a) and (b), the PXD patterns of M10L5FF hydrogenated at 275 and 350 °C under 2.5 MPa are shown. In both cases MgH$_2$ and remnant Mg as well as phases such as LiF and MgF$_2$ are detected. After dehydrogenation, the PXD pattern of M10L5FF (Fig. 2A (c)) shows the presence of Mg, LiF and MgF$_2$. These XRD patterns clearly evidence that the reversible hydride system is Mg/MgH$_2$ and LiF and MgF$_2$ are stable phases. However, the presence of Fe or any phase containing Fe as well as the presence of LiBH$_4$ in the hydrogenated and dehydrogenated samples (Fig. 2A) are not detected.

In Fig. 2B, the DSC curves of M10L, M10L5Fe and M10L5FF can be observed. In all cases (Fig. 2B (a), (b) and (c)), the endothermic event corresponding to LiBH$_4$ structural transition (~120 °C) appears. However, the melting process of LiBH$_4$ (~280 °C) is just observed for M10L (Fig. 2B (a)). It suggests that part of the LiBH$_4$ is still present even after hydrogen cycling. The fact that LiBH$_4$ is not detected in the PXD (Fig. 2A) can be ascribed to its amorphous nature after melting or to the formation of the amorphous LiBH$_{4-y}$F$_y$ phase [28,46,47]. All thermal events between 275 and 400 °C belong to MgH$_2$ decomposition (Fig. 2B (a), (b) and (c)). These multiple peaks are related to the particle size distribution of the Mg−MgH$_2$ agglomerates. This point will be further discussed later.

In order to shed light on the interaction processes occurring during milling and hydrogen cycling, an in-situ SR−PXD experiment with a M40L10FF sample (as−milled Mg + 40 mol% LiBH$_4$ and then 10 mol% of FeF$_3$ mixed with mortar into a glove box − see Table 1) has been performed. In Fig. 3, the in-situ SR−PXD patterns as a function of the temperature and H$_2$ pressure are shown.

At the beginning of the heating process (Fig. 3: ramp from 50 to 350 °C at 0.1 MPa of H$_2$) the structural transition from LiBH$_{4(L.T.)}$ (L.T.: Low temperature) to LiBH$_{4(H.T.)}$ (H.T.: High temperature) at about 115 °C is observed [43,44]. Additionally, the FeF$_3$ peak intensities decrease between 100 and 175 °C. At 150 °C, reflections coming from the formation of LiF start to appear. Then, at about 200 °C, it is noticed that MgH$_2$ is formed. At around 250 °C, LiBH$_{4(H.T.)}$ melts and its reflections disappear [43,44]. The MgH$_2$ reflections start to decrease at about 290 °C. After dwelling for 10 min at 350 °C and 0.1 MPa of H$_2$ pressure, MgH$_2$ is not any longer observed. At the end of the isothermal process at 0.1 MPa of H$_2$, Mg, LiF and MgF$_2$ are only detected. In the last stage of the in-situ SR−PXD measurement (Fig. 3), the H$_2$ pressure has been increased to 5.0 MPa holding the temperature at 350 °C. After two minutes, Mg disappears. Then, only reflections coming from MgH$_2$ as well as from LiF and MgF$_2$ are detected.

The MgH$_2$ peaks at q = 1.9 and q = 2.5 Å^{-1} positions observed during the hydrogenation process (Fig. 3) confirm the MgH$_2$
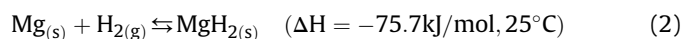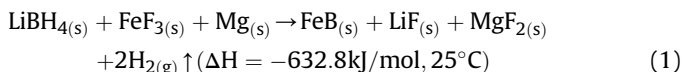

formation−decomposition during heating process (~200 and 350 °C). It is also important to point out that Fe is not detected during the in-situ SR−PXD experiment (Fig. 3) as well as in the PXD after hydrogen cycling (Fig. 2A). This suggests that it can be present as a nanometric Fe containing phase (amorphous to the X-ray).

It is now possible to correlate the results shown in Figs. 1 and 2 with the in-situ SR-PXD experiment (Fig. 3). The DSC curve of M10L5FF after MM (Fig. 1B (c)) exhibits an exothermal event between 90 and 150 °C which can be associated with the interaction between LiBH$_4$ and FeF$_3$ to form LiF as well as the interaction between Mg and FeF$_3$ to form MgF$_2$ (Fig. 2A − PXD after cycling and Fig. 3 − heating under 0.1 MPa H$_2$). Zhang et al. [45] have reported a similar exothermal event for a LiBH$_4$−20 wt% SiO$_2$−30 wt% TiF$_3$, showing not only the formation of LiF but also of TiB$_2$. Moreover, Pranzas et al. [48] have also published for the composite system 2LiBH$_4$ + MgH$_2$ + 0.1NbF$_5$ the formation of NbB$_2$. Thus, the iron boride species formation during heating (Figs. 1B and 3) is not discarded.

The M10L5FF composition has a higher amount of LiBH$_4$ than that of FeF$_3$. Hence, after milling and the first exothermal event (Fig. 1B (c)) remnant LiBH$_4$ is still present. The second endothermic event (Fig. 1B (c)) shows a peak maximum at 280 °C which belongs to the melting of LiBH$_4$. It is noticed that this endothermic event (Fig. 1B (c)) begins at lower temperature than the observed for other materials (Fig. 1B, commercial LiBH$_4$, (a) and (b)). Au et al. [49] have observed that the melting temperature of LiBH$_4$ is modified by the presence of halides. The fluorine ion is able to substitute hydrogen atoms in the LiBH$_4$, so that LiBH$_{4-y}$F$_y$ is formed. This LiBH$_{4-y}$F$_y$ phase might be responsible for the reduced melting temperature of LiBH$_4$ as observed in Fig. 1B (c) [28]. The reduced melting temperature of LiBH$_4$ (Fig. 1B (c)) might be also ascribed to the presence of LiF and MgF$_2$. The bump at 310 °C observed after the LiBH$_4$ melting (Fig. 1B (c)) accounts for the MgH$_2$ decomposition. As seen in Fig. 3, the in-situ formed MgH$_2$ starts to decompose between 300 and 350 °C, which is in agreement with the thermal behavior observed in the DSC curve of M10L5FF (Fig. 1B (c)).

In order to analyze the crystalline and amorphous phases obtained from the Mg, LiBH$_4$ and FeF$_3$ interactions, phase composition equilibrium calculations based on the Gibbs free energy minimization have been carried out with the HSC Chemistry software [42]. The calculations for M10L5FF and M40L10FF compositions and conditions such as MM (25 °C and 100 kPa of Ar), heating and hydrogenation are considered. In all the calculations LiBH$_4$ solid phase is only taken into account and Fe$_2$B is not included. Additionally, the formation of diborane B$_2$H$_6$ in the gas phase is also considered. Table 2 shows the obtained phase equilibrium compositions after MM, hydrogen absorption and desorption.

As seen in Table 2, according to the calculations for both compositions M10L5FF and M40L10FF, after milling and subsequent heating and hydrogenation phases such as MgH$_2$, LiF, MgF$_2$ and FeB are formed. Therefore, the phase equilibrium calculations (Table 2) and the experimental evidence (Figs. 1−3) suggest that during milling and subsequent heating, reaction (1) and (2) can occur.

$$\text{LiBH}_{4(s)} + \text{FeF}_{3(s)} + \text{Mg}_{(s)} \rightarrow \text{FeB}_{(s)} + \text{LiF}_{(s)} + \text{MgF}_{2(s)}$$
$$+ 2\text{H}_{2(g)} \uparrow (\Delta H = -632.8 \text{kJ/mol}, 25°\text{C}) \quad (1)$$

$$\text{Mg}_{(s)} + \text{H}_{2(g)} \leftrightarrows \text{MgH}_{2(s)} \quad (\Delta H = -75.7 \text{kJ/mol}, 25°\text{C}) \quad (2)$$

During milling, part of the LiBH$_4$ interacts with FeF$_3$ thus releasing H$_2$ (reaction (2)). Then, the released H$_2$ reacts with fresh Mg in order to form MgH$_2$ (Fig. 1A (c), B (c) and C, Fig. 3 and reaction (3)). It is important to point out that according to the calculations B$_2$H$_{6(g)}$ is not formed in the gas phase. This result is in concordance
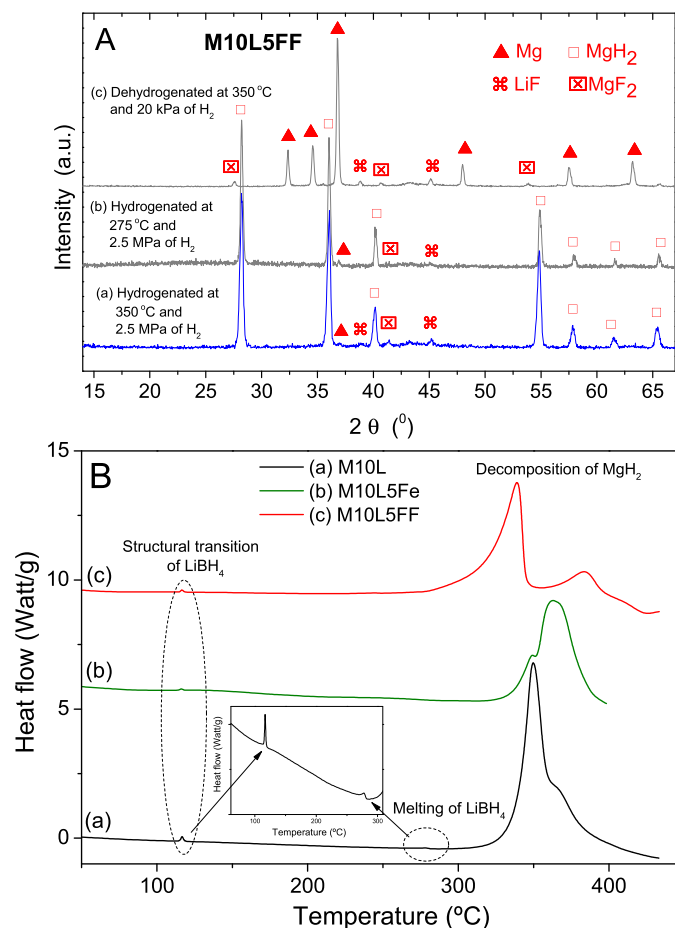
Fig. 2. A − PXD of the M10L5FF material after hydrogenation-dehydrogenation cycling and sample subtracted: (a) hydrogenated at 350 °C and 2.5 MPa of H$_2$, (b) hydrogenated at 275 °C and 2.5 MPa of H$_2$ and (c) dehydrogenated at 350 °C and 20 kPa of H$_2$. B − DSC of samples after hydrogenation-dehydrogenation cycling and sample subtracted: hydrogenated at 275 °C and 2.5 MPa: (a) M10L, (b) M10L5Fe and (c) M10L5FF (5 °C min^{-1} and 122 cm^3 min^{-1} of Ar).
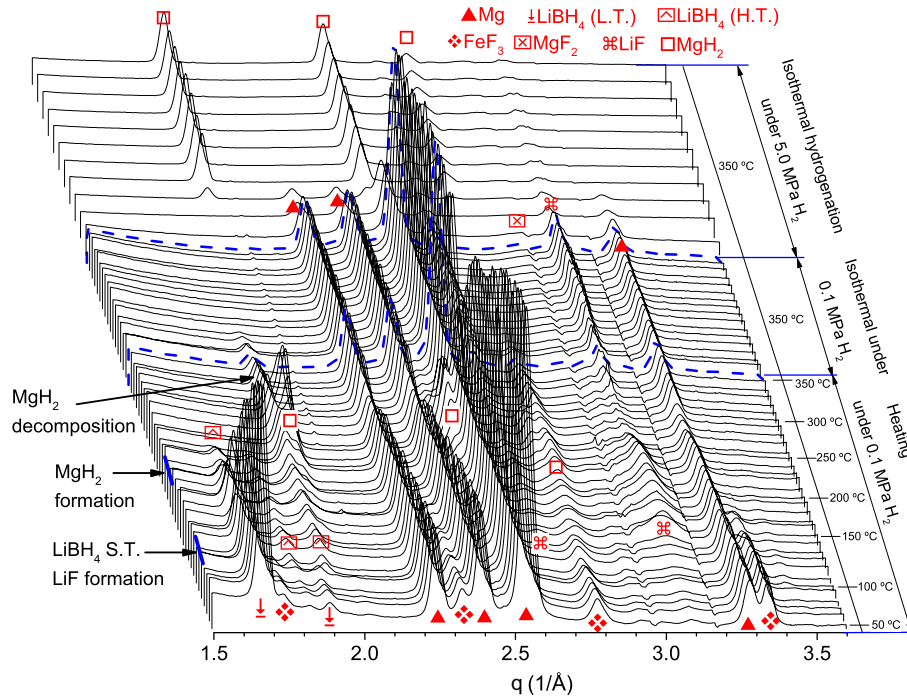
Fig. 3. In-situ SR−PXD for M40L10FF. Heating at 3−4 °C min^{-1} from room temperature to 350 °C under 0.1 MPa of H$_2$. Isothermal at 350 °C under 0.1 MPa of H$_2$ for 40 min. Isothermal hydrogenation at 350 °C under 5.0 MPa of H$_2$. λ = 0.99917 Å. Beamline I711 in the Max-lab, Lund, Sweden. S.T.: Structural transition.

with FT-IR and H$_2$ detection analyses of the milling chamber's gas phase. Hence the reaction between LiBH$_4$ and FeF$_3$ evolves releasing H$_2$ according to reaction (1) and as verified by the leak detector. Then, during heating (DSC curve − Fig. 1B (c), Fig. 3 and reaction (1)), the remnant LiBH$_4$ further reacts with FeF$_3$ modifying its structural transition (exothermic peak between 90 and 150 °C)

and melting (broader endothermic event between 250 °C and 340 °C) temperatures. The observed bump at 310 °C (Fig. 1B (c) and Fig. 3) is related to the MgH$_2$ decomposition (reaction (2)). After hydrogen cycling, PXD and DSC analyses (Fig. 2A and B, Fig. 3, Table 2 − Calculations) show that the Mg/MgH$_2$ system is able to reversible uptake and release hydrogen. Moreover, LiF and MgF$_2$ are seen after heating (Fig. 3), hydrogenation and dehydrogenation (Fig. 2A). This hints at an irreversible formation of these phases as proposed by Zhang et al. for a similar material system [45]. The formation of a transition metal boride species is also proposed in reaction (1). Deng et al. [50] have investigated the 5LiBH$_4$ + Mg$_2$FeH$_6$ composite system. They found that Mg$_2$FeH$_6$ decomposes to provide free Fe. Then, this free Fe reacts with LiBH$_4$

Table 2
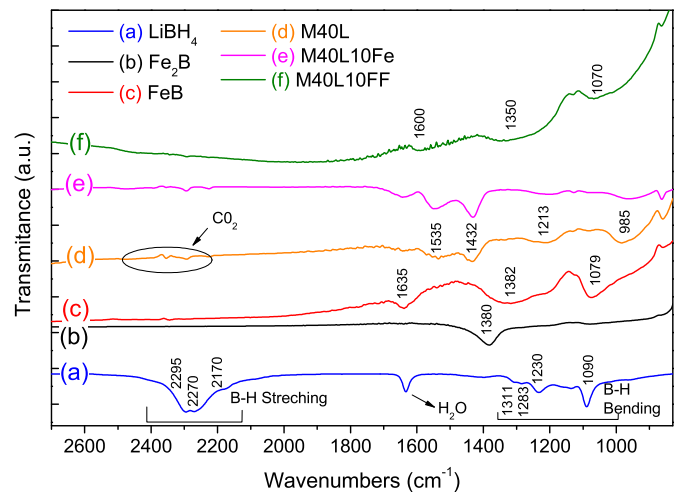Calculated amounts (mol%) of equilibrium phases at 25 °C for M10L5FF and M40L10FF compositions. Conditions: 25 °C under 100 kPa of Ar for MM, from 25 to 350 °C under 100 kPa for heating and 350 °C under 5.0 MPa of H$_2$ for hydrogenation.

Species	Starting compositions	After milling (milling at 25 °C and 100 kPa Ar)	Heating from 25 °C to 350 °C and 100 kPa of Ar	Hydrogenation at 350 °C and 5.0 MPa of H$_2$
M10L5FF				
Mg$_{(S)}$	85	60	79	29
LiBH$_{4(S)}$	10	−	−	−
FeF$_{3(S)}$	5	−	−	−
B$_{(S)}$	−	5	5	5
LiH$_{(S)}$	−	−	−	−
Fe$_{(S)}$	−	−	−	−
LiF$_{(S)}$	−	9	9	9
MgF$_{2(S)}$	−	2	2	2
B$_2$H$_{6(g)}$	−	−	−	−
MgH$_{2(S)}$	−	19	−	50
FeB$_{(S)}$	−	5	5	5
M40L10FF				
Mg$_{(S)}$	50	12	46	11
LiBH$_{4(S)}$	40	16	8	16
FeF$_{3(S)}$	10	−	−	−
B$_{(S)}$	−	9	16	9
LiH$_{(S)}$	−	−	−	−
Fe$_{(S)}$	−	−	−	−
LiF$_{(S)}$	−	17	23	17
MgF$_{2(S)}$	−	4	0.1	4
B$_2$H$_{6(g)}$	−	−	−	−
MgH$_{2(S)}$	−	34	7	35
FeB$_{(S)}$	−	8	7	8

Fig. 4. FT−IR analyses: (a) − commercial LiBH$_4$, (b) − commercial Fe$_2$B, (c) − commercial FeB, (d) − M40L, (e) − M40L10Fe, (f) − M40L10FF.

Table 3
Crystallite size and agglomerate size distribution of Mg/MgH$_2$: Mg (starting material) and the investigated materials: M10L, M10L5Fe and M10L5FF after milling and after hydrogen cycling (hydrogenated samples at 275 °C and 2.5 MPa).

Materials	Crystallite size[a] [nm]	D[v, 0.1][b] [μm]	Volume mean diameter [μm]	D[v, 0.9][c] [μm]
Mg	45	131	198	>200
Materials after milling				
M10L	20	10	52	169
M10L5Fe	20	15	66	132
M10L5FF	20	9	36	70
Materials after hydrogen cycling				
M10L	60	15	62	143
M10L5Fe	70	15	63	138
M10L5FF	40	5	46	134

[a] For the milled materials: crystallite size of Mg (101), 2θ: 36°. For the hydrogen cycled materials: crystallite size of MgH$_2$ (100), 2θ: 28°.

[b] D(v, 0.1) is the size of particle for which 10% of the sample is below this size.

[c] D(v, 0.9) gives a size of particle for which 90% of the sample is below this size.

to form FeB. The presence of FeB species has been detected by PXD after dehydrogenation of the 5LiBH$_4$+Mg$_2$FeH$_6$ composite system at 450 °C during more than 3 h. On the contrary, here, FeB is not observed in the PXD analyses (Figs. 1A (c), 2A and 3). This fact might be related to the formation of nanocrystalline or complete amorphous FeB at relative low temperatures (350 and 275 °C) and during shorter times.

3.2. Solid phase FT–IR analyses of the composite materials

In order to verify the formation of FeB species, FT-IR analyses of the solid phase have been performed. In Fig. 4, FT-IR analyses of the commercial materials (Fig. 4(a−c)) and materials (Fig. 4(d−f)) prepared after a non-isothermal heating up to 450 °C and under 100 kPa of H$_2$ in a Sieverts device can be observed. The material composition for Mg−LiBH$_4$−FeF$_3$ (Fig. 4(f)) is the same as the one used for the in-situ PXD analyses (Fig. 3).

In the case of commercial LiBH$_4$ (Fig. 4(a)), the spectrum shows peaks corresponding to [BH$_4$]$^-$ stretching modes (2295, 2270 and 2170 cm^{-1}) and [BH$_4$]$^-$ bending modes (1311, 1283, 1230 and 1090 cm^{-1}) [51]. Fe$_2$B spectrum (Fig. 4(b)) presents a peak at 1380 cm^{-1} which is not related with any mode. However, FeB spectrum (Fig. 4(c)) shows three peaks at 1079, 1382 and 1635 cm^{-1} [52]. The M40L spectrum (Fig. 4(d)) does not exhibit peaks belonging to the [BH$_4$]$^-$ modes, suggesting that LiBH$_4$ might have decomposed during heating up to 450 °C. As seen, the shape of the FeB spectrum (Fig. 4(c)) is different from the M40L (Fig. 4(d)) and M40L10Fe (Fig. 4(e)) ones. It is not possible to clearly identify the presence of FeB in the M40L10Fe spectrum (Fig. 4(e)), though free Fe would be available to react with LiBH$_4$, resulting in this iron boride species. Nevertheless, the M40L10FF spectrum (Fig. 4(f)) shows peaks at similar positions (1600, 1350 and 1070 cm^{-1}) to those seen in the commercial FeB (1635, 1079, 1382 cm^{-1}, Fig. 4(c)).
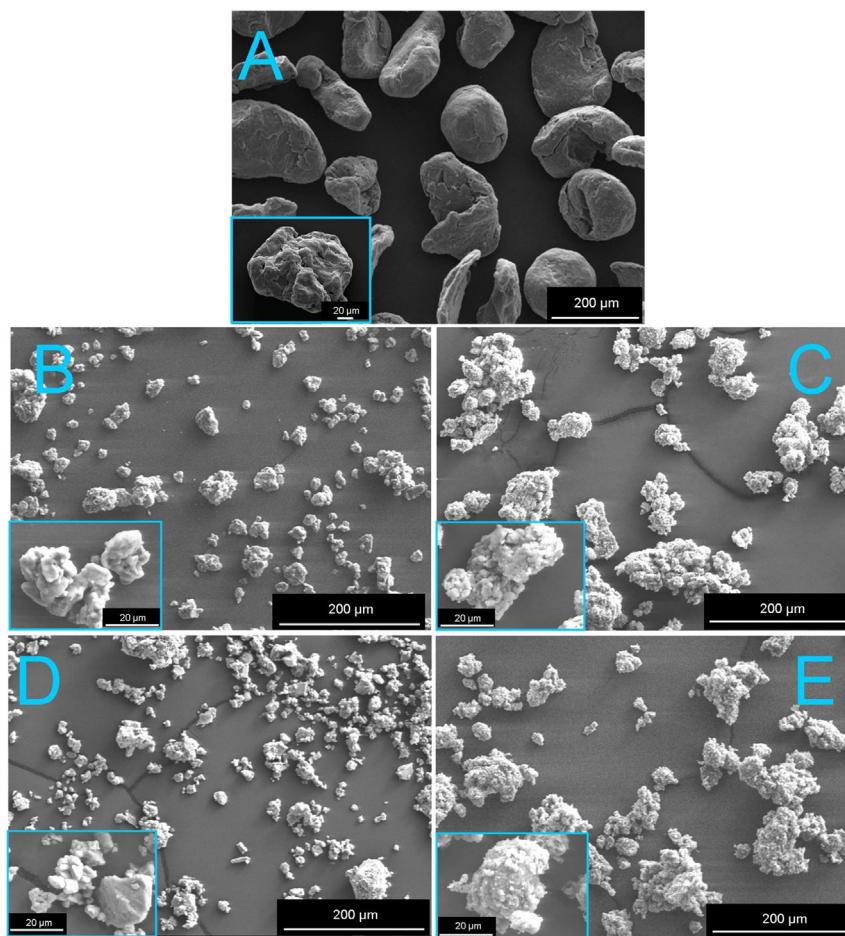

Fig. 5. Secondary electron SEM micrographs of stick mounted samples. Agglomerate size distribution and agglomerate morphology (inset plots): A − Mg (starting material). Materials after milling: B − M10L and D − M10L5FF. Materials after hydrogen cycling: C − M10L and E − M10L5FF.

Therefore, this evidence strongly suggests that FeB is formed in accordance to the proposed reaction (1).

3.3. Studies on the morphology, microstructure and nanostructure

The effects of milling and hydrogen cycling upon the microstructural and morphological characteristics of the Mg-composites materials (M10L, M10L5F and M10L5FF) have been assessed via agglomerate size distribution analyses (named: PSD), crystallite size calculations, SEM micrographs of sticker-mounted and compacted samples and HR-TEM images.

In Table 3 the crystallite sizes of Mg/MgH_2 and the agglomerate size distribution analyses of the materials (M10L, M10L5Fe and M10L5FF) after milling and hydrogen cycling can be seen. The morphology and also agglomerate size distributions of these materials at the same conditions are shown in the sticker-mounted SEM micrographs (Fig. 5).

After milling, the crystallite and agglomerate sizes of Mg are appreciable reduced in comparison with the initial Mg (Table 3 and Fig. 5(A, B and D)). The presence of $LiBH_4$ facilitates the microstructural refinement during milling, resulting in the formation of Mg agglomerates with pits and cracks (Fig. 5(B and D) – inset

plots). These refined and irregular shaped Mg agglomerates provide shorter diffusion paths for hydrogen and more specific surface for the Mg and H interaction [9,10,53,54].

After cycling, the mean agglomerate sizes slightly increase (Table 3—M10L and M10L5FF, Fig. 5(C and E)) or keep almost in the same value (Table 3 – M10L5Fe). It is noted that M10L5FF presents the smallest mean agglomerate size and range of agglomerate size distribution after milling (Mg) and hydrogen cycling (MgH_2); Table 3 and Fig. 5(B–E). Moreover, after cycling the MgH_2 crystallite size of M10L5FF is also the smallest one (Table 3). It is important to make clear that the agglomerate size distributions of the M10L5Fe and M10L5FF materials after cycling (Table 3) leads to hydrogen release behaviors in more than a step. In Fig. 2B (Section 3.1), the observed overlapped endothermic events are related to the size distribution of MgH_2 agglomerates.

Taking into account that FeB particles are not detected by PXD (Figs. 2A and 3) and for this reason it is not possible to have an idea of its size (crystallite size) and morphology (sticker-mounted samples – Fig. 5), SEM analyses with back scattered electrons of compacted samples after hydrogen cycling have been performed. In Fig. 6, compacted powders SEM micrographs with back scattered electrons in an extended region (Fig. 6A–C) and localized region
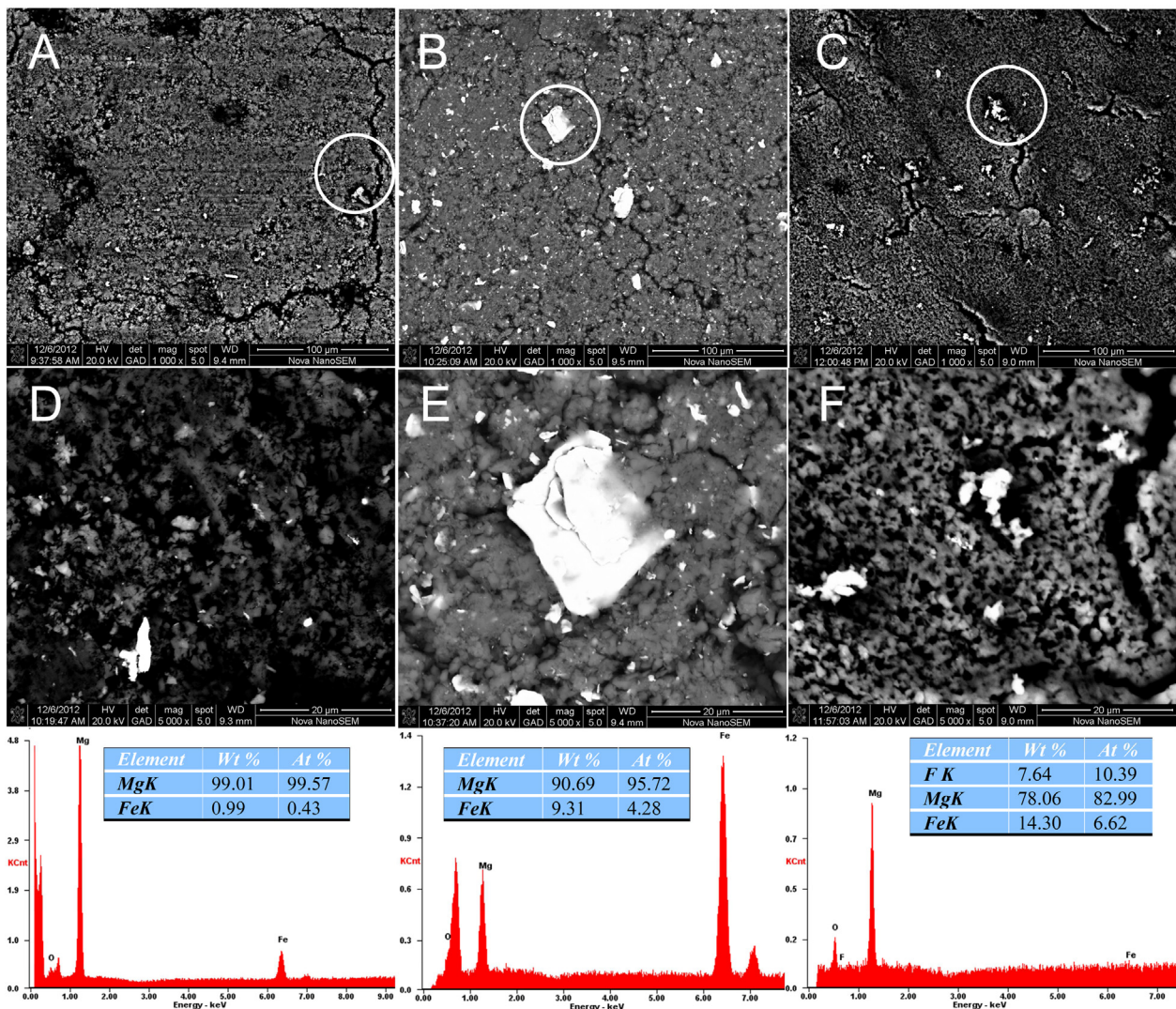

Element	Wt %	At %
MgK	99.01	99.57
FeK	0.99	0.43

Element	Wt %	At %
MgK	90.69	95.72
FeK	9.31	4.28

Element	Wt %	At %
F K	7.64	10.39
MgK	78.06	82.99
FeK	14.30	6.62

Fig. 6. Back-scattered electron SEM images and EDS analyses of compacted powder samples after hydrogen absorption at 275 °C and 2.5 MPa: (A) and (D) M10L, (B) and (E) M10L5Fe, (C) and (F) M10L5FF.

(Fig. 6D–F; indicated with a white circle) with EDS analyses in the indicated localized region can be seen. The bright particles correspond to Fe or Fe compound phase, while the grey backgrounds stand for the Mg matrix.

In the case of M10L sample (Fig. 6(A and D)), it is important to notice that a minimal amount of Fe particles are present in the material (Fig. 6(A and D) and EDS analysis). The presence of Fe particles in the M10L material without intentional addition of Fe can be ascribed to some contamination coming from the grinding medium (stainless steel balls) during milling. For M10L5Fe and M10L5FF material (Fig. 6B, C, E and F and EDS analyses), the bright particles are clearly noticed and detected. In this case the observed bright phase (Fig. 6B, C, E and F) would belong to FeB species. As

noticed (Fig. 6B, C, E and F), the FeB agglomerates are clearly smaller in the M10L5FF material than in the M10L5Fe material. This can be attributed to the simultaneous decomposition and interaction of FeF_3 and $LiBH_4$ which provides reduced size free Fe particles and consequently smaller FeB particles. As mentioned before, this FeB species is not seen by the PXD techniques, suggesting that its diffraction domains have a nanometric range. However, FeB associated with the bright phase (Fig. 6) is clearly seen in a micrometric range. This fact can be attributed to the presence of agglomerates of FeB composed of particles with nanometric domains (short range order domains).

Considering the SEM observations and the nature of the Fe rich phase, HR-TEM and dark field images along with EDS and electron
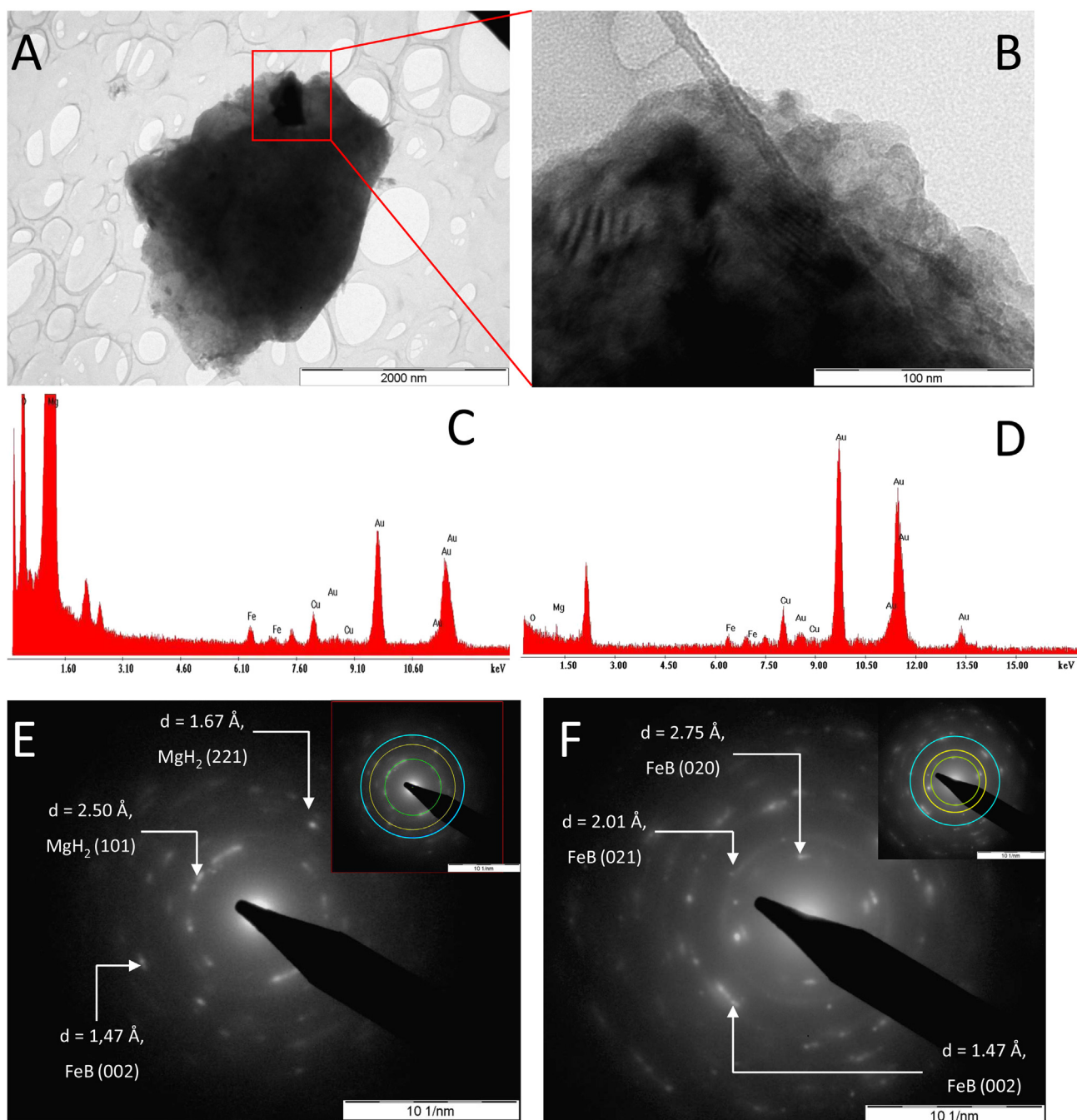

Fig. 7. A and B – HR-TEM images, C and D – EDS analyses, E and F–Electron diffraction patterns for M10L5Fe hydrogenated at 275 °C.

diffraction patterns for the M10L5Fe and M10L5FF samples hydrogenated at 275 °C have been done (Fig. 7 and Fig. 8). In Fig. 7, the HR-TEM images of an extended region, its EDS and electron diffraction pattern for M10L5Fe can be observed (Fig. 7A, C and E). The particles found in the sample range the 200 nm and they present a rather compact morphology (Fig. 7A). The EDS analysis (Fig. 7C) evidences the presence of elemental Mg and Fe (Au and Cu

come from the device and the sample holder, respectively; oxygen comes from the short exposure of the sample to the air). The electron diffraction pattern (Fig. 7E) provides the identification of some rings belonging to MgH_2 and FeB. The same analysis has been performed in a localized region (Fig. 7B — Indicated in Fig. 7A with a red frame). In this case the EDS analysis clearly detects Fe whereas Mg is almost not present (Fig. 7D). This is in agreement with the
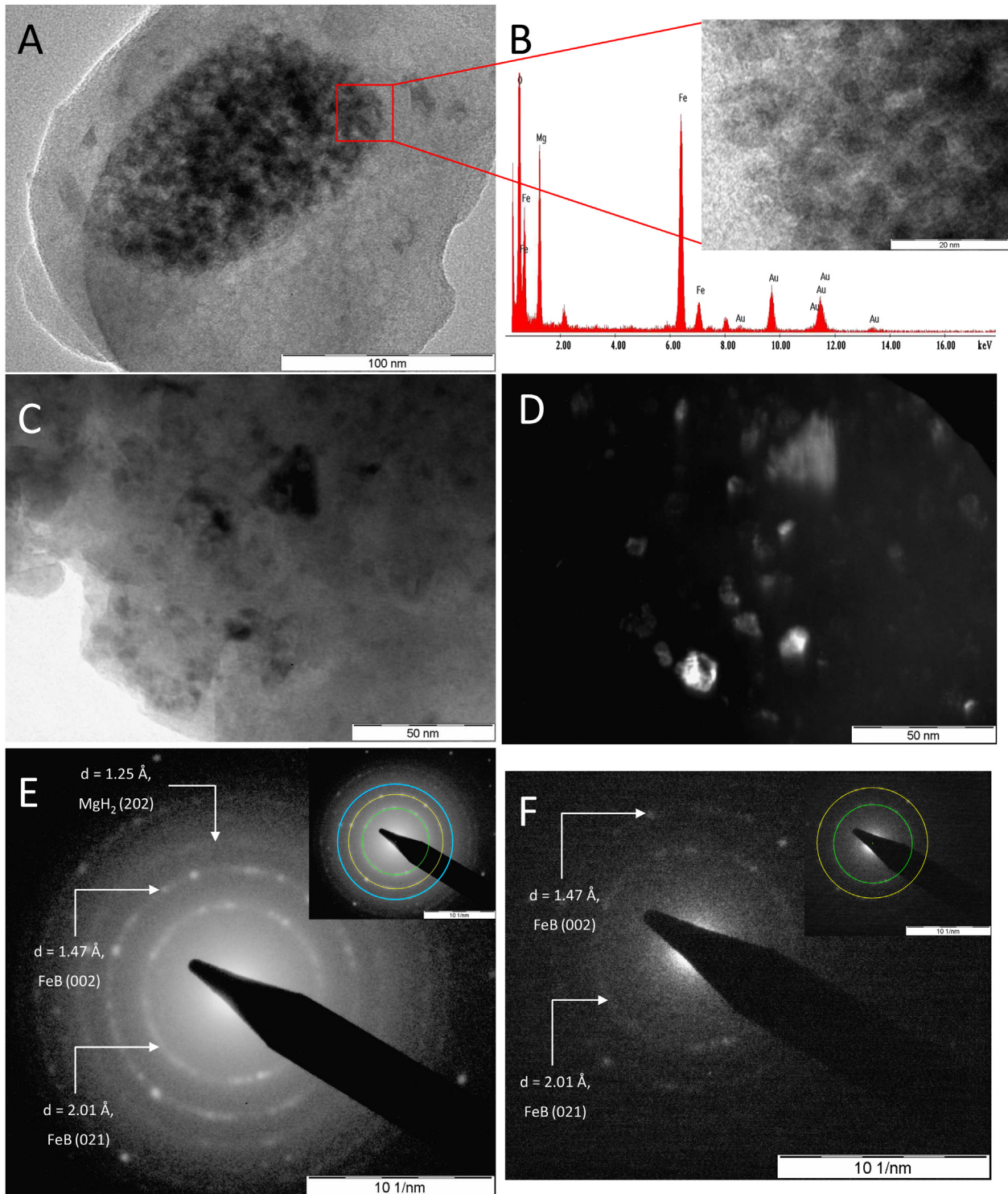

Fig. 8. A and inset plot — HR-TEM images, B — EDS analysis, C — Bright field TEM image, D — Dark field TEM image and E and F — Electron diffraction patterns for M10L5FF hydrogenated at 275 °C.

electron diffraction pattern (Fig. 7F) in which rings which belong to FeB are observed.

Fig. 8 shows HR-TEM and dark field images, EDS and electron diffraction analyses for M10L5FF. Agglomerates of about 100 nm with a non compact morphology are found in the M10L5FF material (Fig. 8A). As seen in the EDS analysis (Fig. 8B), the analyzed agglomerate has elemental Mg and Fe in quite high amount. In the inset plot (HR-TEM image from the red square indicated in Fig. 8A), it is possible to see that this agglomerate is formed by small nanoparticles of sizes between 5 and 10 nm. This kind of non-compact agglomerates and small nanoparticles have been not observed in the M10L5Fe material (Fig. 7). In order to identify the phases, electron diffraction patterns (Fig. 8) have been done. MgH_2 and FeB are identified in Fig. 8E, while just FeB is detected in Fig. 8F. In both electron diffraction patterns (Fig. 8E and F) it is clearly noticed that the rings corresponding to FeB are broad, which indicates that this phase present small sizes. The diffraction pattern (Fig. 8E) corresponding to the bright particles in the dark field image (Fig. 8D) indicates that the observed small nanoparticles (Fig. 8A and inset plot) belong to the FeB species. These results allows to understand the reason why FeB species are not detected by the PXD (Figs. 2A and 3) and the nature of the micrometric agglomerate seen by SEM (Fig. 6). For M10L5Fe these micrometric (Fig. 6E) and nanometric (Fig. 7) agglomerates are rather compact, while for M10L5FF are not (Fig. 6F – micrometric and Fig. 8 – nanometric). This support the idea of having micrometric agglomerates composed of small nanoparticles that are eventually seen by SEM and not detected by PXD because of the short range crystalline domains.

The in-situ formation–decomposition of MgH_2 during milling (Fig. 1A (c) and B (c)), the formation of stable phases such as LiF, MgF_2 and FeB (Fig. 1A (c) and B (c), Figs. 2A and 3) upon heating and subsequent hydrogen cycling account for the further microstructural refinement of the M10L5FF material (Table 3). During hydrogen cycling, the formed stable phases can act as pinning centers of the phase boundaries precluding the Mg agglomeration, so that small agglomerate as well as crystallite sizes (see Table 3) are retained. Furthermore, some rare earth and metal transition borides can act as catalyst for the MgH_2 [55,56]. Thus, the presence

of the nanoparticles of FeB forming non-compact agglomerates composed of small nanometric particles (Fig. 8) might have influence in the kinetic behavior of hydrogen release in the studied materials.

3.4. Study of the kinetic desorption behavior of the composite material

The kinetic behavior of the M10L, M10L5Fe and M10L5FF materials has been assessed after heating up to 350 °C, then successive stabilization hydrogen cycles at 350 °C and subsequent hydrogenation-dehydrogenation cycles at 325, 300 and 275 °C. In Fig. 9, the hydrogen sorption curves of M10L, M10L5Fe and M10L5FF at 275 °C are shown. During the first heating, for M10L5Fe and M10L5FF, stable phases are formed (as explained in Section 3.1) leading to a slight reduction of the hydrogen capacity. Throughout hydrogen cycling, the reversible hydride system is Mg/MgH_2 and all materials show stable hydrogen capacity (same wt% observed in Fig. 9) which means that they have good stability to about 8–10 hydrogen cycles.

In the case of the hydrogen uptake (Fig. 9A), the rates do not practically exhibit any differences. The absorption time to reach 80% of the full hydrogen capacity is about 5 min in all cases (Fig. 9A). It is also noticed that the hydrogen capacity is reduced because of the Fe and FeF_3 addition (Fig. 7A (b and c)). However, hydrogen capacities are far larger than for pure Mg at 275 °C [10]. The improved hydrogen capacities and faster hydrogen uptake rates are ascribed to the refined microstructure (small crystallites and agglomerate sizes of Mg and irregular shape Mg agglomerates [9]). On the contrary, the addition of FeF_3 noticeable improves the hydrogen release rate from MgH_2 (Fig. 9B). The M10L5FF material can reversible release near 5 wt.% H in about 100 min (Fig. 9B (c)).

In order to elucidate whether the FeF_3 addition has a catalytic effect upon the MgH_2 decomposition, the decomposition activation energy values (E_a) by the Kissinger method have been calculated [39]. Fig. 10 shows the Kissinger plots and their corresponding DSC curves (inset plots) for M10L, M10L5Fe and M10L5FF hydrogenated at 275 °C and 2.5 MPa. In all cases, the E_a values are calculated from the larger DSC peak, discarding a bump or smaller second peak
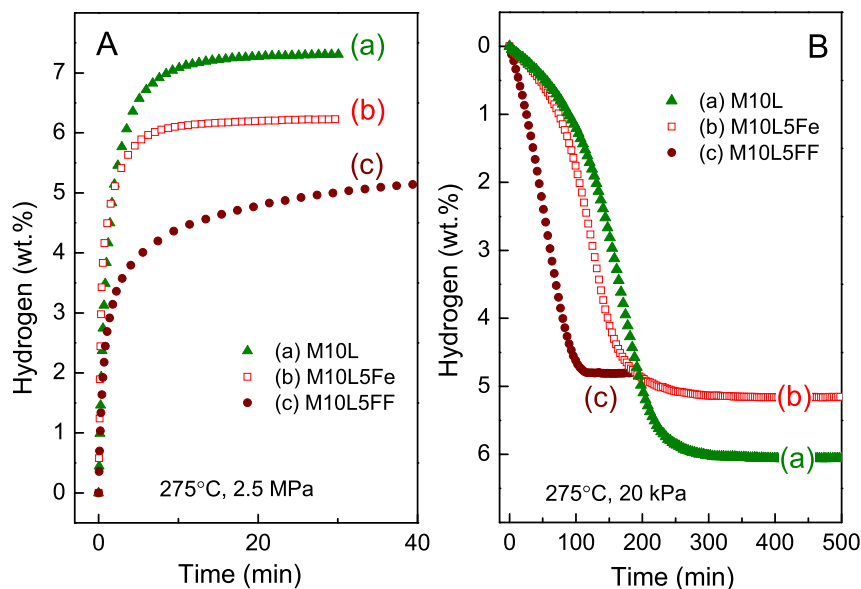

Fig. 9. Hydrogen sorption curves: A – Hydrogen absorption curves at 275 °C and 2.5 MPa and B – Hydrogen desorption curves at 275 °C and 20 kPa for (a) M10L, (b) M10L5Fe, (c) M10L5FF.
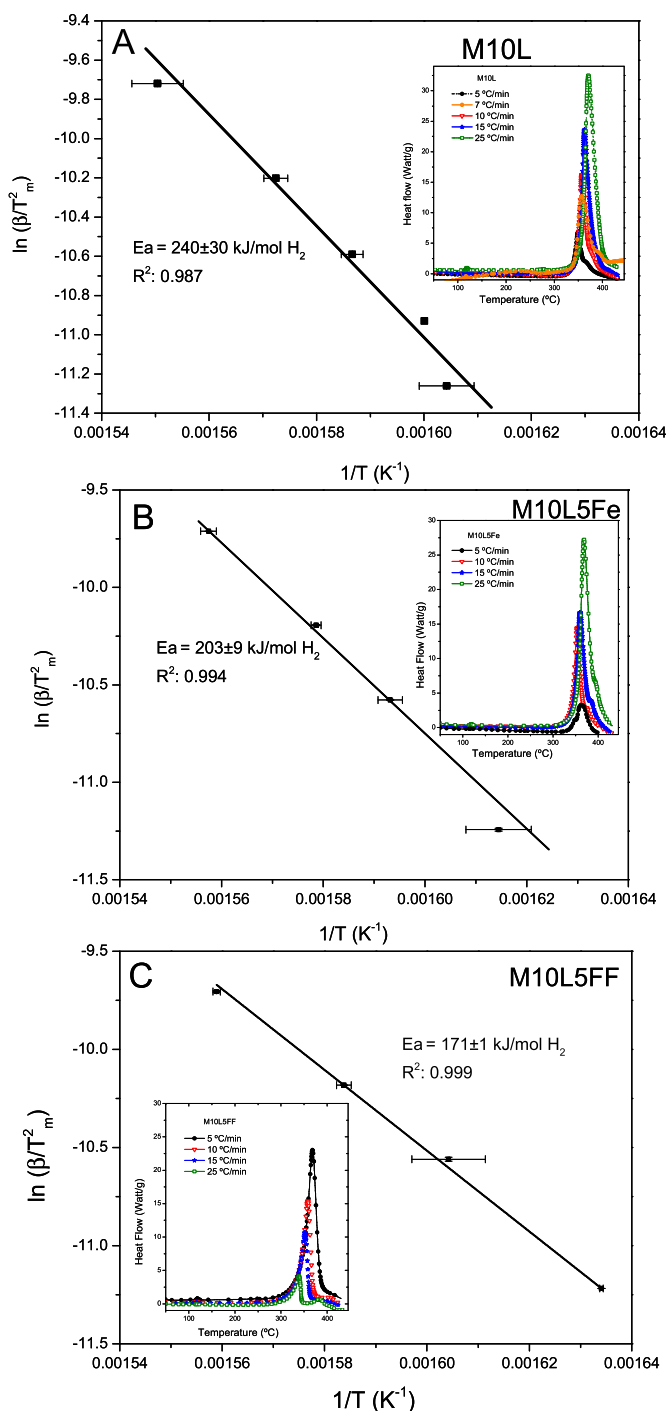
Fig. 10. Decomposition activation energy (Ea) plots and DSC curves (inset plots) for the materials after hydrogen cycling and hydrogenation at 275 °C and 2.5 MPa: A − M10L, B − M10L5Fe and C − M10L5FF.

related to the desorption behavior of a small proportion of the sample. Consequently, the larger DSC peaks are considered more representative for E_a calculations.

As seen in Fig. 10, the E_a for both M10L and M10L5Fe are overlapped, 240 ± 30 and 203 ± 9 kJ mol^{-1} of H$_2$, respectively. Thus, the addition of Fe has no significant effect upon the hydrogen release. This result also reflects the similar hydrogen desorption rates observed in Fig. 9B (a and b). On the other hand, the addition of FeF$_3$ clearly reduces the measured E_a (171 ± 1 kJ mol^{-1} H$_2$ for

M10L5FF $< 203 \pm 9$ kJ mol^{-1} of H$_2$ for M10L5Fe and 240 ± 30 kJ mol^{-1} of H$_2$ for M10L), reflecting an enhanced hydrogen desorption kinetic (Fig. 7(B)).

This fact can be attributed to two main factors. First, the microstructural refinement: additional Mg agglomerate size reduction during milling (Fig. 5 and Table 3) and subsequent formation of irreversible phases (MgF$_2$, LiF and FeB). These irreversible phases can act as pinning centers for the grain boundaries leading to a stabilization of the smaller crystallite sizes and changing the surface properties and the cohesion energies of MgH$_2$/Mg agglomerates, thereby hindering their further growth. Second, the presence of nanometric and well dispersed particles of FeB species, resulting from the interaction between FeF$_3$ and LiBH$_4$ during milling, heating and hydrogen cycling. Considering that FeB species has an electronic structure in which Fe−Fe and Fe−B bonds have metallic character, the oxidation state of Fe is the same as the metallic Fe [57−60]. It suggests that the well dispersed FeB nanoparticles might have a catalytic effect on the MgH$_2$ decomposition as transition metals such as Fe have [1,2]. In the case of M10L5Fe, the SEM and TEM results indicate that the found FeB agglomerates are rather compact and the particles rather bigger and not well dispersed, precluding an effective beneficial effect for the dehydrogenation Ea of the Mg/MgH$_2$.

4. Conclusions

The addition of FeF$_3$ to Mg−LiBH$_4$ composite has been investigated. Upon milling and subsequent heating, the Mg−LiBH$_4$−FeF$_3$ interactions result in Mg agglomerates with reduced sizes and irregular shapes and the formation of stable phases (MgF$_2$, LiF and FeB). On one hand, the reduced irregular shaped Mg agglomerates provide shorter diffusion paths for the hydrogen diffusion, resulting in larger hydrogen capacities and faster hydrogen uptake rates. On the other hand, the in-situ formed stable phases act as pinning centers for the grain boundaries precluding the further Mg/MgH$_2$ agglomeration and retaining the microstructural refinement during hydrogen cycling. Moreover, nanometric and well dispersed FeB, which might act as catalytic species, is present in the M10L5FF material. These characteristics lead to a reduction in the activation energy of dehydrogenation of about 60 kJ mol^{-1} of H$_2$ and allows to reach about 5 wt% H reversible capacity in reduced hydrogen desorption times at a low temperature of 275 °C.

References

[1] A. Seayad, D.M. Antonelli, Adv. Mater. 16 (9−10) (2004) 765−777.
[2] M. Fichtner, Adv. Eng. Mater. 7 (2005) 443−455.
[3] B. Sakintuna, F. Lamari-Darkrim, M. Hirscher, Int. J. Hydrogen Energy 32 (2007) 1121−1140.
[4] S.-I. Orimo, Y. Nakamori, J.R. Eliseo, A. Züttel, C.M. Jensen, Chem. Rev. 107 (2007) 4111−4132.
[5] H.-W. Li, Y. Yan, S.-I. Orimo, A. Züttel, et al., Energies 4 (2011) 185−214.

[6] J.M. Pasini, C. Corgnale, B.A. van Hassel, T. Motyka, et al., Int. J. Hydrogen Energy 38 (2013) 9755–9765.
[7] United States Department of Energy, Targets for Onboard Hydrogen Storage Systems for Light-Duty Vehicles. Revision 4.0, 2009. http://www1.eere.energy.gov/hydrogenandfuelcells/storage/pdfs/targets_onboard_hydro_storage.pdf.
[8] G. Liang, J. Huot, S. Boily, A. Van Neste, R. Schulz, J. Alloys Compd. 292 (1999) 247–252.
[9] N. Hanada, T. Ichikawa, H. Fujii, J. Phys. Chem. B 109 (2005) 7188–7194.
[10] G. Barkhordarian, T. Klassen, R. Bormann, J. Alloys Compd. 407 (2006) 249–255.
[11] W. Luo, J. Alloys Compd. 381 (2004) 284–287.
[12] S. Orimo, Y. Nakamori, G. Kitahara, K. Miwa, N. Ohba, S. Towata, A. Züttel, J. Alloys Compd. 404–406 (2005) 417–430.
[13] S.R. Johnson, P.A. Anderson, P.P. Edwards, I. Gameson, J.W. Prendergast, M. Al-Mamouri, et al., Chem. Commun. 22 (2005) 2823–2825.
[14] J.F. Mao, Z. Wu, T.J. Chen, B.C. Weng, N.X. Xu, T.S. Huang, et al., J. Phys. Chem. C 111 (2007) 12495–12498.
[15] X.B. Yu, D.M. Grant, G.S. Walker, Chem. Commun. 37 (2006) 3906–3908.
[16] J.A. Puszkiel, F.C. Gennari, Scr. Mater. 60 (2009) 667–660.
[17] J.A. Puszkiel, PhD Thesis, Universidad Nacional de Cuyo, Instituto Balseiro, 2012. http://ricabib.cab.cnea.gov.ar/328/.
[18] M. Dornheim, N. Eigen, G. Barkhordarian, T. Klassen, R. Bormann, Adv. Eng. Mater. 8 (2006) 377–385.
[19] W. Oelerich, T. Klassen, R. Bormann, J. Alloys Compds. 315 (2000) 237–242.
[20] G. Barkhordarian, T. Klassen, R. Bormann, Scr. Mater. 49 (2003) 213–217.
[21] G. Barkhordarian, T. Klassen, R. Bormann, J. Alloys Compds. 364 (2004) 242–246.
[22] L. Xie, Y. Liu, Y.T. Wang, J. Zheng, X.G. Li, Scr. Mater. 55 (2007) 4585–4591.
[23] S. Deledda, A. Borissova, C. Poinsignon, W.J. Botta, M. Dornheim, T. Klassen, J. Alloys Compd. 404–406 (2005) 409–412.
[24] A.R. Yavari, A. LeMoulec, F.R. de Castro, S. Deledda, O. Friedrichs, W.J. Botta, et al., Scr. Mater. 52 (2005) 719–724.
[25] F.-J. Liu, S. Suda, J. Alloys Compd. 231 (1995) 742–750.
[26] S.-A. Jin, J.-H. Shim, Y.W. Cho, K.-W. Yi, J. Power Sources 172 (2007) 859–862.
[27] S.-A. Jin, J.-H. Shim, J.-P. Ahn, Y.W. Cho, K.-W. Yi, Scr. Mater. 55 (2007) 5073–5079.
[28] I.E. Malka, T. Czujko, J. Bystrzycki, Int. J. Hydrogen Energy 35 (2010) 1706–1712.
[29] I.E. Malka, J. Bystrzycki, T. Płocinski, T. Czujko, J. Alloys Compd. 509S (2011) S616–S620.
[30] L.-P. Ma, X.-D. Kang, H.-B. Dai, Y. Liang, Z.-Z. Fang, P.-J. Wang, et al., Scr. Mater. 57 (2009) 2250–2258.
[31] G. Barkhordarian, T. Klassen, R. Bormann, J. Phys. Chem. B 110 (2006) 11020–11024.
[32] M. Au, A. Jurgensen, K. Zeigler, J. Phys. Chem. B 110 (2006) 26482–26487.
[33] Z.Z. Fang, L.P. Ma, X.D. Kang, P.J. Wang, P. Wang, H.M. Cheng, Appl. Phys. Lett. 94 (2009), 044104 (1–3).
[34] Z.Z. Fang, X.-D. Kang, Z.-X. Yang, G.S. Walker, P. Wang, J. Phys. Chem. C 115 (2011) 11839–11845.
[35] F.F. Fang, Y. Li, Y. Song, D. Sun, Q. Zhang, L. Ouyang, et al., J. Phys. Chem. C 115 (2011) 13528–13533.
[36] L. Alexander, P.H. Klug, J. Appl. Phys. 21 (1950) 137–142.
[37] Y. Cerenius, K. Staal, L.A. Svensson, T. Usby, A. Oskasson, J. Albertson, et al., J. Synchrotron Rad. 7 (2000) 1–399.
[38] T.R. Jensen, T.K. Nielsen, Y. Filinchuck, J.E. Jørgensen, Y. Cerenius, M.E. Gray, et al., J. Appl. Cryst. 43 (2010) 1456–1463.
[39] H.E. Kissinger, Anal. Chem. 29 (1957) 1702–1706.
[40] G. Meyer, D.S. Rodríguez, F. Castro, G. Fernández, Hydrogen energy progress, in: Proceedings of the 11th World Energy Conference, Stuttgart, Germany, 1293, 1996.
[41] G. Liang, J. Huot, S. Boily, R. Schulz, J. Alloys Compd. 305 (2000) 239–245.
[42] H.S.C. Outokumpu, Chemistry for Windows, Version 6.0, Outokumpu Research Oy, Pori, Findland, 2009.
[43] E.M. Fedneva, V.L. Alpatova, V.I. Mikheeva, Transl. Zh. Neorg. Khim. Russ. J. Inorg. Chem. 9 (6) (1964) 826–827.
[44] T. Nakagawa, T. Ichikawa, H. Hanada, Y. Kojima, H. Fujii, J. Alloys Compd. 446–447 (2007) 306–309.
[45] Y. Zhang, W. Zhang, M.–Q. Fan, S.–S. Liu, H.–L. Chu, Y.–H. Zhang, et al., J. Phys. Chem. C 112 (10) (2008) 4005–4010.
[46] R. Gosalawit-Utke, J.M. Bellosta von Colbe, M. Dornheim, T.R. Jensen, Y. Cerenius, C. Bonatto Minella, et al., J. Phys. Chem. C 114 (22) (2010) 10291–10296.
[47] I. Saldan, J.M. Ramallo-López, F.G. Requejo, K. Suarez-Alcantara, J.M. Bellosta von Colbe, J. Avila, Int. J. Hydrogen Energy 37 (2012) 10236–10239.
[48] P.K. Pranzas, U. Bösenberg, F. Karimi, M. Münning, O. Metz, C.B. Minella, et al., Adv. Eng. Mater. 13 (8) (2011) 730–736.
[49] M. Au, A. Jurgensen, W.A. Spencer, D.L. Anton, F.E. Pinkerton, S.-J. Hwang, et al., J. Phys. Chem. C 112 (2008) 18661–18671.
[50] S. Deng, X. Xiao, L. Han, Y. Li, S. Li, H. Ge, et al., Int. J. Hydrogen Energy 37 (2012) 6733–6740.
[51] T.J. Marks, J.R. Kolb, Chem. Rev. 77 (2) (1977) 263–293.
[52] K. Molvinger, M. Lopez, J. Court, P.Y. Chavant, Appl. Catal. A 231 (2002) 91–98.
[53] P.K. Pranzas, M. Dornheim, U. Bosenberg, J.R. Ares Fernandez, G. Goerigk, S.V. Roth, et al., J. Appl. Cryst. 40 (s1) (2007) s383–s387.
[54] F. Karimi, P.K. Pranzas, A. Hoell, U. Vainio, E. Welter, V.S. Raghuwanshi, et al., J. Appl. Cryst. 47 (2014), http://dx.doi.org/10.1107/S1600576713031567.
[55] F.C. Gennari, J.A. Puszkiel, J. Power Sources 195 (2010) 3266–3274.
[56] F. Cova, P. Arneodo Larochette, F. Gennari, Int. J. Hydrogen Energy 37 (2012) 15210–15219.
[57] D.J. Joyner, O. Johnson, M.-D. Hercules, J. Phys. F. Metal. Phys. 10 (1980) 169–180.
[58] O. Johnson, D.J. Joyner, M.-D. Hercules, J. Am. Chem. Soc. 84 (1980) 542–547.
[59] D.J. Joyner, O. Johnson, M.D. Hercules, M.D. Bullet, J.H. Weaver, J. Phys. Rev. B 24 (1981) 3122–3137.
[60] G. Li, D. Wangi, J. Phys. Condens. Matter 1 (1989) 1799–1808.